*R*esearch in
*A*stronomy and
*A*strophysics

Modeling the rail surface unevenness of a high-precision radio telescope

Na Li, Peng Li, Jiang Wu and Bao-Yan Duan

School of Mechanical and Electronic Engineering, Xidian University, Xi'an 710071, China;
lina@mail.xidian.edu.cn, yinhong0523@163.com, 836640638@qq.com, byduan@xidian.edu.cn

Abstract This study proposed a coarse-fine mixed model for describing the rail surface unevenness of an ultra-large fully steerable radio telescope (Qi Tai Telescope) with a diameter of 110 meters. The rail surface unevenness includes information on error arising from two different scales, i.e., the long-period-short-change and the short-period-long-change. Consequently, in this study an idea of a mixed model was proposed, in which trigonometric and fractal functions were, respectively, used to describe information on error from two scales. Key parameters were determined by using the least squares method and the wavelet transform method, and finally, a specific mathematical expression of the model was obtained by optimization. To validate the effectiveness of the new modeling method, the mixed model was then used to describe the rails of the Green Bank Telescope, the Large Millimeter Telescope, and a radio telescope in Miyun, Beijing. A comparative study revealed that the maximum error was less than 15%, thus the result was superior to those of existing modeling methods.

Key words: magnetic fields — radiation mechanisms: general — instrumentation: adaptive optics — methods: numerical — telescopes

1 INTRODUCTION

Throughout the past several decades, many countries have been racing to construct large telescopes for radio astronomy observation, such as the Green Bank Telescope (GBT) with a 100×110 m off-set aperture located in West Virginia (Symmes et al. 2008), the Effelsberg Telescope with a 100 m aperture located in Germany (Wielebinski et al. 2011) and the Sardinia Radio Telescope with a 64 m aperture located in Italy (Bolli et al. 2015). China plans to build the Qi Tai Telescope with a 110 m aperture in Xinjiang, in the northwest part of China, which would be the world's largest aperture fully steerable radio telescope. It would be primarily used for investigating the formation and evolution of stars, the formation of dark matter in the universe, observation of pulsars and exploration of deep space based on very long baseline interferometry. All the above mentioned large radio telescopes have large volumes and are extremely heavy; however, they also set high demands for pointing accuracy (Kaercher 2004b). As modern radio telescopes increase in scale and weight, the use of a rotary table antenna pedestal encounters a series of prob-

lems in design, manufacturing technology, transport and cost. However, the aforementioned problems can be mitigated by using a wheel-track antenna pedestal in which some components, such as big gear wheels and foundations, can be omitted (Juneja et al. 2006).

Currently, most high-precision radio telescopes have adopted completely-welded rails. Compared to non-welded rails, the rails using complete welding technology can avoid large deformation at rail junctions; thereby significantly prolonging the service lives of the junctions. However, during the manufacturing and welding processes, generation of errors such as surface roughness and rail stress deformation is inevitable (Deng & Murakawa 2008). These errors are collectively referred to as rail unevenness. The unevenness can directly affect the pointing accuracy of antennas (Antebi & Kan 2003; Smith 2006). As early as 2000, Gawronski et al. investigated the effects of unevenness of rails on the pointing accuracy of an antenna. Using an inclinometer, they converted measured unevenness data to the corresponding errors in the antenna's azimuth and pitch angles via a geometric relationship (Gawronski et al. 2000). Moreover, Tonino Pisanu et al. considered the combined effect of

the deformation of the azimuth housing induced by rail unevenness and temperature drift on the pointing accuracy (Pisanu et al. 2010). Furthermore, some researchers also indirectly introduced non-linear errors from the rails into the antenna's pointing error model (Matsuzawa et al. 2014). Therefore, the effect of rail unevenness on the pointing accuracy of the antenna should be investigated based on an accurate model of rail unevenness. Although the above-described studies have achieved fruitful results, they still lack precise descriptions of rail unevenness, thus leading to large fitting errors. As a result, the fitting residual errors can severely affect the antenna's ultimate pointing accuracy.

Regarding modeling rail unevenness, Okubo et al. numerically analyzed test data and demonstrated that the unevenness was stationary and normalized (Okubo et al. 2002). Kong et al. proposed a prediction model for rail unevenness, capable of predicting amplitude variations of each sampling point along the rail during a period of time (Kong et al. 2014). Furthermore, by taking rail unevenness into account, Belov et al. put forward a method for correcting the pointing accuracy of a radio telescope (Belov et al. 1997). Finally, Zhang et al. proposed a prediction scheme for surface roughness, and constructed the influencing model of machining technology on surface roughness (Zhang et al. 2009). The above-described studies have laid the foundations for modeling rail unevenness; however, some key problems still exist (Guiar et al. 1986). Studies involving modeling rail unevenness have primarily used the model's characteristic indexes as reference, and the model lacked comparisons with practical surface conditions. Due to the multi-scale aspects and randomness in unevenness, a unified high-precision mathematical model on the unevenness of a high-precision antenna rail is still lacking.

Aimed at solving the aforementioned problems, and based on measured unevenness data, in this study large-scale and small-scale error information on surface unevenness is described using a trigonometric function and a fractal function, respectively, and a mixed description model is proposed in an innovative way. After experimental verification, the constructed model can meet the engineering requirements for accuracy.

2 MODELING THE LARGE-SCALE ERRORS IN THE RAIL SURFACE

The errors that lead to radio telescope rail unevenness primarily originate from the following two aspects: surface roughness produced in the machining process of a single rail and deformations produced during the horizontal adjustment welding process and post-processing.

The friction of the cutting tool or abrasive, plastic deformations and metal tearing in chip-separation, and high-frequency vibrations in the machining system during a single rail's machining process lead to the appearance of various microscopic geometries with different shapes and sizes on the rail surface (Ambrosini et al. 2013). The surface roughness can be described by several characteristics, such as randomness, high frequency, low amplitude and small scale (Zhou et al. 1993).

On the other hand, many processing methods, such as preheating before welding, temperature control in the process, stress release during welding and heat processing, are required in order to prevent the appearance of delayed cracks as well as to eliminate quenched structures in the material's heat affected zone after welding. These processes may lead to rail deformation due to uneven stress distribution (Pisanu et al. 2010). These deformations exhibit systematization, low frequencies and large amplitudes (Deng & Kiyoshima 2012).

According to characteristics of the distribution, large-scale errors on the rail surface can be regarded as the superposition of harmonic waves at different frequencies. A Fourier series is a common periodic function and can be conveniently used to describe large-scale errors (Hu & Tonder 1992). Such a Fourier series can be written as follows:

$$
\begin{aligned}
f_1(x) &= A_0 + \sum_{n=1}^{m} A_n \sin(n\omega x + \theta_n) \\
&= A_0 + \sum_{n=1}^{m} a_n \sin(n\omega x) + b_n \cos(n\omega x) \quad (1) \\
&= A_0 + a_1\varphi_1(x) + b_1\phi_1(x) + \cdots \\
&\quad + a_n\varphi_n(x) + b_n\phi_n(x),
\end{aligned}
$$

where

$$a_n \sin(n\omega x) = A_n \sin(n\omega x)\cos(\theta_n),$$

$$b_n \cos(n\omega t) = A_n \cos(n\omega t)\sin(\theta_n);$$

x denotes the rail's position; ω denotes the fundamental frequency; n denotes the number of times a waveform of $\sin(n\omega x + \theta_n)$ appears within the sampling length; m denotes the expansion order of the Fourier series with the value range of $[1, N/2]$; and

$$\varphi_n(x) = \sin(n\omega x)$$

and

$$\phi_n(x) = \cos(n\omega x).$$

Equation (1) includes the undetermined parameter A_0 in the measured data describing the unevenness

(x_i, y_i). Key parameters of the function are determined by the least squares method when fitting the model (Qiao & Liu 2013). Furthermore, $f_1(x)$ was selected to minimize

$$\sum_{i=1}^{N} (y_i - \tilde{y}_i)^2 = \sum_{i=1}^{N} (y_i - f_1(x_i))^2,$$

which can approximately represent a linear combination of constant coefficients in many functions

$$\phi_1(x), \varphi_1(x), \cdots, \phi_n(x), \varphi_n(x),$$

as shown in Equation (2). Thus, N equations were obtained for the determination of A_0, a_1, b_1, $\cdots$, a_n and b_n.

$$y_i = A_0 + a_1\varphi_1(x_i) + b_1\phi_1(x_i) + \cdots + a_n\varphi_n(x_i) \\ + b_n\phi_n(x_i) \, i = 1, \cdots, N. \tag{2}$$

The observed values always include errors, and the effect of accidental errors can be reduced by utilizing a large number of observations. Therefore, an overdetermined set of linear equations is used in Equation (3), if

$$A = \begin{bmatrix} 1 & \varphi_1(x_1) & \cdots & \varphi_m(x_1) & \phi_1(x_1) & \cdots & \phi_m(x_1) \\ \vdots & \vdots & \vdots & \vdots & \vdots & \vdots & \vdots \\ 1 & \varphi_1(x_N) & \cdots & \varphi_m(x_N) & \phi_1(x_N) & \cdots & \phi_m(x_m) \end{bmatrix}_{N \times (2m+1)}, B = \begin{bmatrix} y_1 \\ \vdots \\ y_N \end{bmatrix}, X = \begin{bmatrix} A_0 \\ a_1 \\ \vdots \\ a_m \\ b_1 \\ \vdots \\ b_m \end{bmatrix}, AX = B. \tag{3}$$

The number of equations in the overdetermined set shown in Equation (3) is greater than the number of unknowns ($N > 2m + 1$). Therefore, when the rank of the augmented matrix exceeds the rank of the coefficient matrix, the equation has no solution, and only generalized solutions of the equation can be determined, namely, the least squares solutions. The least squares solutions of A_0, a_1, b_1, $\cdots$, a_n and b_n can make the following Equation (4) minimal

$$F(A_0, a_1, b_1 \cdots a_n, b_n) = \sum_{i=1}^{N} [A_0 + a_1\varphi_1(x_i) + b_1\phi_1(x_i) + \cdots + a_n\varphi_n(x_i) + b_n\phi_n(x_i) - y_i]^2. \tag{4}$$

Therefore, A_0, a_1, b_1, $\cdots$, a_n and b_n should satisfy the following conditions:

$$\frac{\partial F(A_0, a_1, b_1 \cdots a_n, b_n)}{\partial A_0} = 0,$$
$$\frac{\partial F(A_0, a_1, b_1 \cdots a_n, b_n)}{\partial a_i} = 0, \tag{5}$$
$$\frac{\partial F(A_0, a_1, b_1 \cdots a_n, b_n)}{\partial b_i} = 0.$$

To rewrite Equation (5) in the form of a matrix, a set of equations with a coefficient matrix in the form of a square matrix can be obtained

$$A^{\mathrm{T}}AX = A^{\mathrm{T}}B, \tag{6}$$
$$X = (A^{\mathrm{T}}A)^{-1}A^{\mathrm{T}}B. \tag{7}$$

3 MODELING THE SMALL-SCALE ERRORS IN THE RAIL SURFACE

Due to the random, high-frequency and low-amplitude characteristics of small-scale errors on the rail sur-

face, a fractal function was used. Mandelbrot proposed a function to describe a fractal curve based on the Weierstrass function, which is referred to as the Weierstrass-Mandelbrot function (W-M function) and can be written as follows (Majumdar & Bhushan 1990; Mandelbrot 1982)

$$f_2(x) = A^{(D-1)} \sum_{n=n1}^{M} \frac{\cos 2\pi\gamma^n x}{\gamma^{(2-D)n}}, \tag{8}$$

in which $f_2(x)$ denotes the height of the random surface profile; x denotes the position coordinates of the

surface profile; A denotes the amplitude coefficient; D denotes the fractal dimension; γ^n denotes the frequencies of each harmonic wave on the surface; n is the reciprocal of the wavelength (i.e., $\gamma^n = 1/\lambda_n$) and determines the frequency spectrum of the surface; and n_1 corresponds to the minimum cut-off frequency of the surface profile ω_1. Specifically, A determines the size of $f_2(x)$. D is an intrinsic parameter that can reflect the essential characteristics of roughness and is irrelevant with regard to resolution of measuring instruments (Berry & Lewis 1980). Thus, D can describe irregularity of the fractal

function at all scales and its value ranges from 1 to 2 in Equation (8). The value range of γ^n depends on the sampling length L and the maximum resolution of sampling (also known as the cut-off frequency); also $\gamma > 1$. The maximum frequency ω_M is determined by using the Nyquist frequency as follows

$$\omega_1 = \gamma^{n_1} = 1/L,$$
$$\omega_M = \gamma^M = N\gamma^{n_1}/2, \tag{9}$$

where N denotes the number of sample points, and the value range of n is from n_1 to M.

Table 1 summarizes a comparison of five methods used for determining key parameters of the fractal function, where M1, M2, M3, M4 and M5 represent the power spectrum method, the structure function method, the root mean square of the profile method, the box-counting dimension method and the wavelet method, respectively. A comparison of the result shows that the wavelet method exhibits the highest precision corresponding to a dimension of 1.3–1.9. Therefore, wavelet analysis was selected as the tool in this study. The Morlet wavelet is a non-orthogonal wavelet and it is smooth and continuous, which is suitable for time series analysis (Arneodo 1996). Based on the Morlet wavelet, the wavelet transform model of the W-M function can be written as follows

$$W_{W-M}(\omega_0, a, b) = \frac{\sqrt{a2\pi}}{2} A^{D-1} \sum_{n=n_1}^{m} \frac{e^{-\frac{1}{2}\omega_0^2 - 2(\pi\gamma^n a)^2} e^{\omega_0 * 2\pi\gamma^n a + j2\pi\gamma^n b}}{\gamma^{(2-D)n}}$$

$$= \frac{\sqrt{a2\pi}}{2} A^{D-1} \sum_{n=n_1}^{m} \frac{e^{-\frac{1}{2}\left(\omega_0^- 2(\pi\gamma^n a)\right)^2} e^{j2\pi\gamma^n b}}{\gamma^{(2-D)n}}. \tag{10}$$

When $\omega_0 = 2\pi\gamma^{ni}a$, $W_{W-M}(\omega_0, a, b)$ has a maximum value. When $n \neq n_i$, $e^{-\frac{1}{2}(\omega_0 - 2(\pi\gamma^n a))^2}$ tends toward zero, and the modulus value of $W_{W-M}(\omega_0, a, b)$ is

$$|W_{W-M}(\omega_0, a, b)| \approx \frac{\sqrt{a2\pi}}{2} \frac{A^{D-1}}{\gamma^{(2-D)n}}. \tag{11}$$

By taking the double logarithm on Equation (11), the following formulations can be obtained

$$\ln(|W_{W-M}(\omega_0, a, b)|) = \ln(\frac{\sqrt{a * 2\pi}}{2}) + (D-1)\ln A + (2-D)\ln(2a\pi) - (2-D)\ln(\omega_0). \tag{12}$$

Furthermore, it can be found that $\ln(|W_{W-M}(\omega_0, a, b)|)$ is directly proportional to $\ln(\omega_0)$. Assuming that the slope is denoted as k, the fractal dimension D and the amplitude coefficient A are obtained as follows

$$D = 2 + k, \tag{13}$$

$$A = e^{\frac{\ln(|W_{W-M}(1,a,b)|) - \ln(\frac{\sqrt{a*2\pi}}{2}) - (2-D)\ln(2a\pi)}{(D-1)}}. \tag{14}$$

Figure 1 shows an example of fractal dimension D of the surface roughness based on a wavelet transform. According to multiple experimental results, when the scale factor was set as 2 ($a = 2$), the result was ideal. As shown in Equation (12), the height of the peak point is irrelevant to the displacement factor b in theory. However, in consideration of errors that may be produced in practical calculations, modulus values of the wavelet transform using several displacement factors b were calculated in our study, and the average value was adopted as the final result.

4 COARSE-FINE MIXED MODELING OF THE RAIL SURFACE

Based on the above-described modeling methods, the large-scale profile of rail unevenness was fitted using a Fourier series. Next, the W-M fractal function was used to describe the fitting residual error, and then the small-scale fitting function was applied. Finally, the coarse-fine mixed model of rail unevenness can be established as shown below in Equation (15):

$$
\begin{aligned}
F(x) &= f_1(x) + \sum_{i=1}^{k} f_2^i(A_i, D_i, L_i, x_0^i, y_0^i) \\
&= \left(a_0 + \sum_{n=1}^{m} \left[a_n \cos(n\omega_0 x) + b_n \sin(n\omega_0 x) \right] \right) + \left(\sum_{i=1}^{k} f_2^i(A_i, D_i, L_i, x_0^i, y_0^i) \right), \\
f_2^i(A_i, D_i, L_i, x_0^i, y_0^i) &= A_i^{(D_i-1)} \sum_{j=n_{1i}}^{M_i} \frac{1}{\gamma^{(2-D_i)j}} \cos\left(2\pi\gamma^j(x + x_0^i) \right) + y_0^i \\
n_{1i} &= \ln(1/L_i)/\ln(\gamma) \\
M_i &= \ln(N\gamma^{n_{1i}}/2)/\ln(\gamma).
\end{aligned}
\tag{15}
$$

Here RMS_m denotes the result of the Fourier series; $a_0, a_1, \cdots, a_n, b_1, \cdots, b_n$ are the undetermined coefficients of $f_1(x)$; m is the expansion order of $f_1(x)$; ω_0 is the fundamental frequency of $f_1(x)$; S is the rail length described by $F(x)$ and is generally set as one third of the rail's overall length; k is the number of rail segments when the W-M fractal function is used for fitting rail unevenness; l is the fitting length of f_2^i ($k = S/l$) and is set as a round number; $f_2^i(A_i, D_i, L_i, x_0^i, y_0^i)$ is the ith segment of the W-M fractal function $f_2(x)$; A_i is the amplitude coefficient of $f_2(x)$, which reflects the value of f_2^i and determines the specific size of f_2^i; L_i is the sampling length of $f_2(x)$; D_i is the fractal dimension of $A_{\min} < A_R < A_{\max}$; and y_0^i and x_0^i are the longitudinal and lateral displacements of $f_2(x)$, respectively.

Equation (15) shows that the Fourier series $0 < x < \infty$ and the W-M fractal function $f_2(x)$ codetermine the fitting precision of rail unevenness. Moreover, the higher the expansion order of the Fourier series (m) is, the higher the fitting precision. Similarly, the shorter the sampling length of W-M fractal function (L) is, the higher the fitting precision. In this study, the sampling length of the W-M fractal function (L) equals the fitting length of the small-scale function, and thus determination of the values of m and L is the key study to determining the unevenness model. The determination methods for these two key parameters are described in detail below. The optimization model based on the W-M fractal function can be described as follows:

$$
f_2(x) = A^{(D-1)} \sum_{n=n1}^{M} \frac{1}{\gamma^{(2-D)n}} \cos(2\pi\gamma^n(x + \Delta x)) + \Delta y,
\tag{16}
$$

$$
\begin{aligned}
\text{Find} \quad & y = (A_i, D_i, L_i, x_0^i, y_0^i)^{\mathrm{T}}, \\
\text{Min.} \quad & F(y) = \sqrt{[\sum_{j=1}^{N} (f_2^i(x_j, y) - y(x_j))^2]/N} \\
\text{S.T.} \quad & x_{\min} < x_0^i < x_{\max}, \\
& L_{\min} < L_i < L_{\max}, \\
& y_{\min} < y_0^i < y_{\max}, \\
& A_{\min} < A_2^i < A_{\max}, \\
& D_{\min} < D_i < D_{\max}.
\end{aligned}
\tag{17}
$$

The upper and lower limits of the variables are determined based on their physical meanings. The physical meanings and the determination methods for the related parameters in the optimization model of the fractal function are described in Figure 2.

5 EXPERIMENTS AND VERIFICATION

In order to validate the effectiveness of the proposed mixed model, the rails of GBT in West Virginia, the Large Millimeter Telescope (LMT) in Mexico (Kaercher 2004a), and a radio telescope in Miyun, Beijing were used as typical cases (Jin et al. 2003). The GBT antenna has an aperture of 100 m, a rail diameter of 64 m, 48 rail segments, an overall length of 201 m, and the unevenness degree (in terms of root mean square (RMS)) is 0.0568 mm. The LMT antenna has an aperture of 50 m, a rail diameter of 39.6 m, 20 rail segments, an overall length of 124.4 m, and the RMS is 0.1697 mm. The antenna in Miyun has an aperture of 32.5 m, a rail diameter of 32.5 m, 20 rail segments, an overall length of 102.1 m, and the RMS is 0.3136 mm.
Requirement 1 is

$$\left| \frac{\mathrm{RMS}_{m-1} - \mathrm{RMS}_m}{\mathrm{RMS}_{m-1}} \right| \le \varepsilon_1, \qquad \varepsilon_1 = 2\%.$$

When expansion orders of the Fourier series are m and $m + 1$, the rail measurement data (x_i, y_i) are fitted, and RMS_{m-1} and RMS_m are the RMS of fitting residuals for two rails.
Requirement 2 is

$$\left| \frac{\mathrm{RMS}'_m}{\mathrm{RMS}_1} \right| \le \varepsilon_2, \quad \varepsilon_2 = 25\%.$$

RMS'_m is the fitting residual of the fractal function in the optimization model. When Requirement 1 is met, the value of m, l and related parameters of $f_1(x)$ are determined, and RMS_1 is the fitting residual of $f_1(x)$.
Requirement 3 is

$$\left| \frac{\mathrm{RMS}_m}{\mathrm{RMS}_0} \right| \le \varepsilon_3, \qquad \varepsilon_3 = 15\%,$$

where RMS_0 is the RMS of the original rail.

Using the correlation coefficient test method (Yan et al. 2012), the non-scaling ranges of three objects under study (GBT, LMT, and Miyun) were calculated, which are $[0.116, 0.901]$, $[0.243, 1.361]$ and $[0.263, 1.156]$, respectively. Then, by using a wavelet transform, the fractal dimensions of three objects were calculated, which are

$$D_{\mathrm{GBT}} = 1.602, \quad D_{\mathrm{LMT}} = 1.568, \quad D_{\mathrm{MY}} = 1.521.$$

(A) The fractal dimension D_i reflects the complexity of the actual rail surface. First, the value of D_i was estimated using a wavelet transform, and then the upper and lower limits of D_i in the optimization model were set.

(B) Then, the value range of amplitude A was approximately calculated according to Equation (18). The amplitude coefficient A_R of the actual rail surface was included in the $[D_{\min}, D_{\max}]$ range; moreover,

$$A_{\min} < A_R < A_{\max}.$$

$$A = e^{\frac{\ln(|W_{W-M}(1,a,b)|) - \ln(\frac{\sqrt{a*2\pi}}{2}) - (2-D)\ln(2a\pi)}{(D-1)}}. \quad (18)$$

(C) The sampling length L should be within the non-scaling range. When L exceeds this non-scaling range, the rail surface morphology does not exhibit any obvious fractal characteristics or may not even have any fractal characteristics. Therefore, the sampling length is equal to the fitting length of the fractal function.

(D) With regard to the longitudinal displacement of fractal function y_0,

$$y_{\min} < y_0 < y_{\max},$$

$$y_{\min} = y_{i\,\min}$$

and

$$y_{\max} = y_{i\,\max},$$

in which $y_{i\,\min}$ and $y_{i\,\max}$ denote the minimum and maximum values of the measured data of y_i respectively. Therefore, the existence of y_0 can be guaranteed so that

$$f_2^i(x)_{i\,\min} < y_{i\,\min}, \quad y_{\max} < f_2^i(x)_{\max}.$$

(E) x_0 represents lateral displacement of the fractal function. In order to determine the most appropriate segment to simulate rail unevenness in the original W-M fractal function, the range of independent variable x in the fractal function is $0 < x < \infty$ in theory; therefore, $0 < x_0 < x_{\max}$ in which $x_{\max}$ is 100 times the fitting length L.

The rails set high demands on the pointing accuracy; therefore, we set $\varepsilon_1 = 2\%, \varepsilon_2 = 1/4$ and $\varepsilon_3 = 20\%$.

Figures 3–5 show local unevenness of the rails for the three basic antennas, and Table 2 lists the RMS values and amplitude ranges of the expansion order for the Fourier series (m), the fitting length of the fractal function (l) and the description error of rail unevenness. Clearly, the amplitude range of the description error is
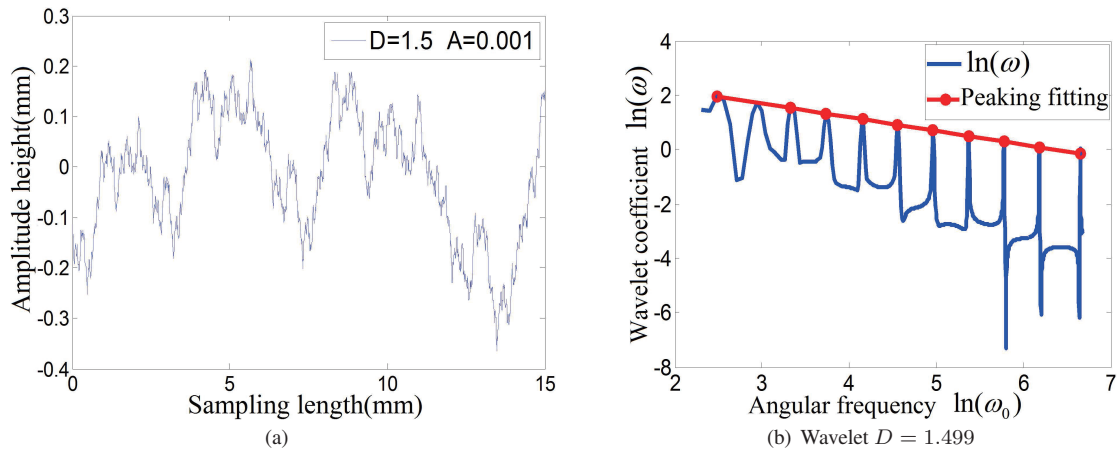
(a)

(b) Wavelet $D = 1.499$

Fig. 1 The fractal dimension D obtained by wavelet analysis. (a) Fractal $D = 1.5$; (b) Wavelet $D = 1.499$.
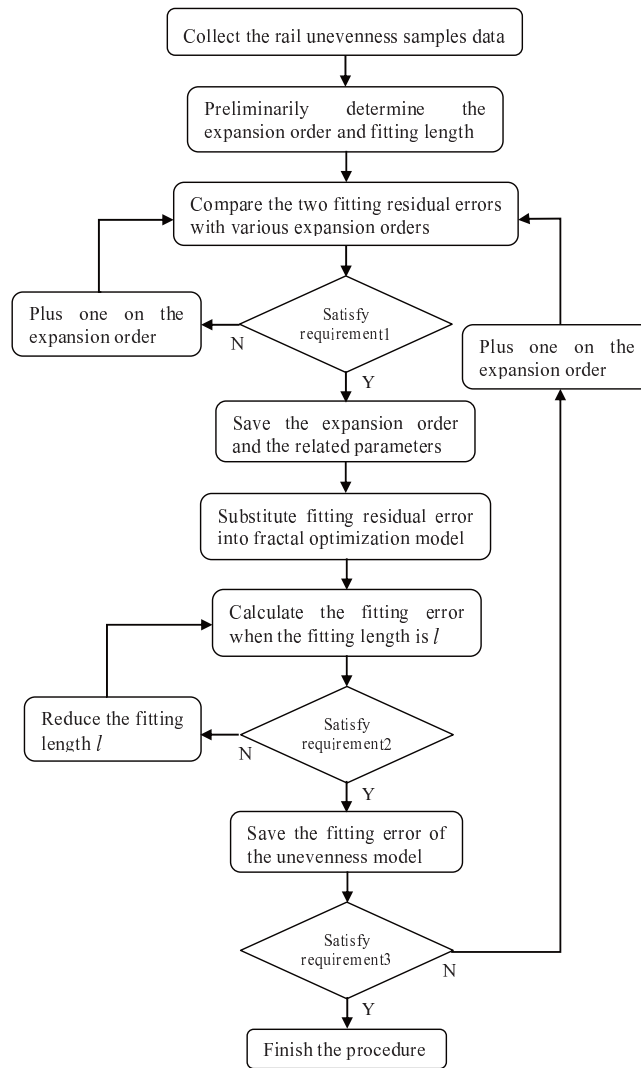

Fig. 2 Flowchart of the detailed process for determination of the parameters.

Table 1 Comparison of Fractal's Key Parameters by Five Methods

Theoretical value of D	Method	D	Error	Relative error (%)
	M1	0.89	0.41	31.54
	M2	1.39	0.09	6.92
1.3	M3	1.43	0.13	10.00
	M4	1.19	0.11	8.46
	M5	1.31	0.01	0.77
	M1	1.43	0.17	10.63
	M2	1.58	0.02	1.25
1.6	M3	1.62	0.02	1.25
	M4	1.32	0.27	16.87
	M5	1.595	0.005	0.31
	M1	1.91	0.01	0.53
	M2	1.54	0.36	18.95
1.9	M3	1.78	0.12	6.32
	M4	1.44	0.46	23.21
	M5	1.89	0.01	0.53

Table 2 Related Parameters and Indexes of Three Different Antennas

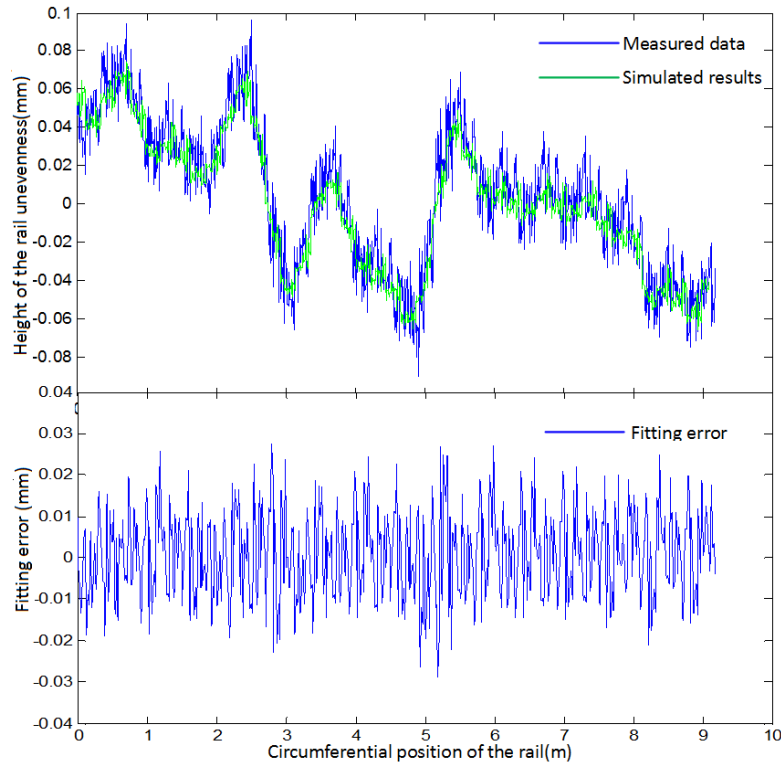|	m	l	RMS_0	RMS_m	B_0	B_m
GBT	18	60	0.0568	0.0107	± 0.2	± 0.02
LMT	20	50	0.1697	0.0273	± 0.4	± 0.06
Miyun	17	50	0.3136	0.0301	± 0.6	± 0.08

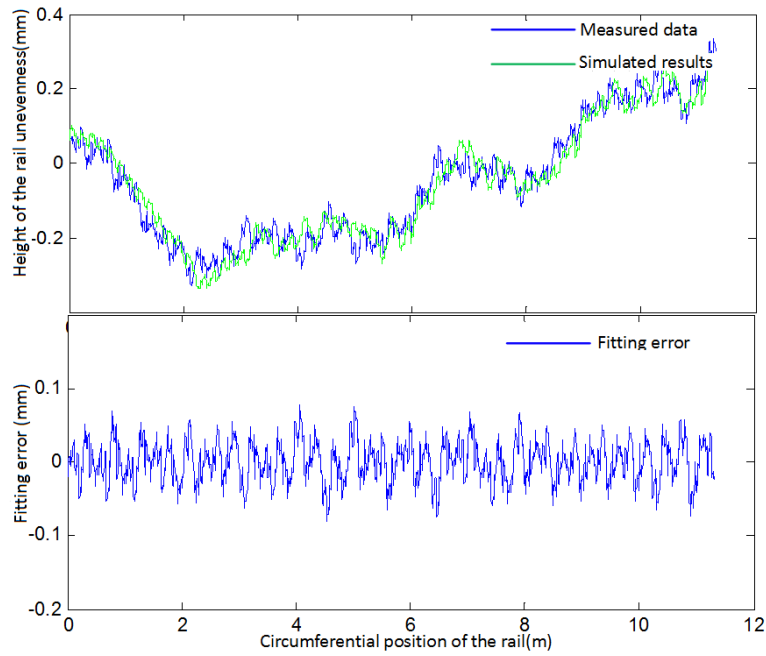**Fig. 3** Comparative study on rail unevenness of the GBT antenna.

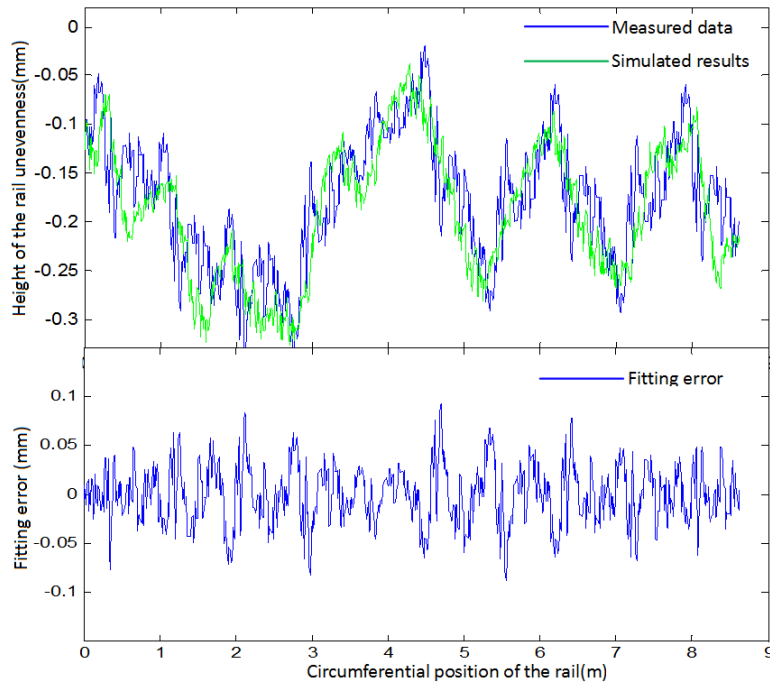**Fig. 4** Comparative study on rail unevenness of the LMT antenna.

Fig. 5 Comparative study on rail unevenness of the antenna in Miyun.

reduced by one order compared to the measured value of rail unevenness.

In Table 2, RMS_0 denotes the RMS value of unevenness for the original rail, RMS_m denotes the RMS value for the fitting error, B_0 denotes the amplitude of unevenness for the original rail and B_m denotes the amplitude of the fitting error. The results of the comparative study revealed that the accuracy of the mixed model was less than 15%, which was superior to those of existing modeling methods.

6 CONCLUSIONS

Based on multi-scale characteristics of rail unevenness, the Fourier series was introduced to describe the large scale surface error and the W-M fractal function for the small scale one. The coarse-fine mixed description model of rail unevenness was proposed. The model could accurately describe the macroscopic outline of the rail surface as well as reflect the rail's microscopic morphology. For verification, the mixed model was applied to describe rail unevenness for the GBT, LMT and a radio telescope in Miyun, Beijing, and satisfactory results were obtained. Undeniably, many more systematic explorations are needed in order to investigate the influence of the relation describing pointing accuracy based on the rail unevenness model, which will be pursued in future studies.

References

Ambrosini, R., Bocchinu, A., Bolli, P., et al. 2013, in Electromagnetics in Advanced Applications (ICEAA), 2013 International Conference on, IEEE, 82

Antebi, J., & Kan, F. W. 2003, in Astronomical Telescopes and Instrumentation, International Society for Optics and Photonics, eds. J. Angel, P. Roger and R. Gilmozzi, 612

Arneodo, A. 1996, Wavelet Analysis of Fractals: from the Mathematical Concepts to Experimental Reality, Wavelets: Theory and Application (New York: Oxford University Press)

Belov, Y., Naumov, A., Chernikova, S., Poperchenko, B., & Sapozhnikov, B. 1997, in Antennas and Propagation Society International Symposium, 1997, 1, IEEE, 568

Berry, M., & Lewis, Z. 1980 in Proceedings of the Royal Society of London, 370

Bolli, P., Orlati, A., Stringhetti, L., et al. 2015, Journal of Astronomical Instrumentation, 4, 1550008

Deng, D., & Murakawa, H. 2008, Computational Materials Science, 43, 353

Deng, D., & Kiyoshima, S. 2012, Computational Materials Science, 62, 23

Gawronski, W., Baher, F., & Quintero, O. 2000, IEEE Antennas and Propagation Magazine, 42, 28

Guiar, C., Lansing, F., & Riggs, R. 1986, TDA Progress Report 4288, JPL/NASA, 02, 36

Hu, Y., & Tonder, K. 1992, International Journal of Machine Tools and Manufacture, 32, 83

Jin, C., Wang, H., & Zhang, X. 2003, Acta Astronomica Sinica, 44, 27

Juneja, G., Kan, F. W., & Antebi, J. 2006, in Proc. SPIE, 6273, Optomechanical Technologies for Astronomy, eds. E. A. Ettedgui, J. Antebi, D. Lemke, 627318

Kaercher, H. J. 2004a, in Proc. SPIE, 5495, Astronomical Structures and Mechanisms Technology, eds. J. Antebi & D. Lemke, 67

Kaercher, H. J. 2004b, in Proc. SPIE, 5382, Second Backaskog Workshop on Extremely Large Telescopes, eds. A. L. Ardeberg & T. Andersen, 233

Kong, D.-Q., Wang, S.-G., Wang, J.-Q., Wang, M., & Zhang, H.-B. 2014, RAA (Research in Astronomy and Astrophysics), 14, 733

Majumdar, A., & Bhushan, B. 1990, Journal of tribology, 112, 205

Mandelbrot, B. B. 1982, The Fractal Geometry of Nature (San Francisco: Freeman)

Matsuzawa, A., Saito, M., Iguchi, S., Nakanishi, K., & Saito, H. 2014, in Proc. SPIE, 9145, Ground-based and Airborne Telescopes V, 91451Z

Okubo, H., Kawai, E., Kondo, T., et al. 2002, IVS CRL-TDC News, 11, 13

Pisanu, T., Buffa, F., Morsiani, M., Pernechele, C., & Poppi, S. 2010, in Proc. SPIE, 7739, Modern Technologies in Space- and Ground-based Telescopes and Instrumentation, eds. E. A. Ettedgui and D. Lemke, 773935

Qiao, B., & Liu, S. 2013, Fractals, 21, 1350018

Smith, D. R. 2006, in Proc. SPIE, 6273, Optomechanical Technologies for Astronomy, eds. E. A. Ettedgui, J. Antebi and D. Lemke, 627314

Symmes, A., Anderson, R., & Egan, D. 2008, in SPIE Astronomical Telescopes+ Instrumentation, International Society for Optics and Photonics, 701238

Wielebinski, R., Junkes, N., & Grahl, B. H. 2011, Journal of Astronomical History and Heritage, 14, 3

Yan, X. J., Xue, L. F., & Li, W. Q. 2012, in Advanced Materials Research, 569, Trans Tech Publ, 88

Zhang, X.-Z., Zhu, X.-Y., Kong, D.-Q., et al. 2009, RAA (Research in Astronomy and Astrophysics), 9, 367

Zhou, G., Leu, M.-C., & Blackmore, D. 1993, Wear, 170, 1